

# Modeling Proton Jumps in HY Zeolite: Effects of Acid Site Heterogeneity

Usha Viswanathan,<sup>†</sup> Justin T. Fermann,<sup>†</sup> Leanna K. Toy,<sup>†</sup> Scott M. Auerbach,<sup>\*,†,‡</sup> Thom Vreven,<sup>§</sup> and Michael J. Frisch<sup>§</sup>

Department of Chemistry and Department of Chemical Engineering, University of Massachusetts Amherst, Amherst, Massachusetts 01003, and Gaussian, Inc., 340 Quinpiac Street Building 40, Wallingford, Connecticut 06492

Received: July 27, 2007; In Final Form: September 21, 2007

We have computed the total mean rate coefficient for proton transfer in bare H–Y zeolite, for comparison with NMR experiments and previous calculations. We computed proton-transfer energies using two-layer ONIOM calculations on an 8T–53T cluster, where  $xT$  indicates  $x$  tetrahedral atoms. Rate coefficients were computed using truncated harmonic semiclassical transition state theory. The zero-point energy (ZPE) corrected proton site energies in H–Y (FAU structure) were found to be O3 (0 kJ mol<sup>-1</sup>), O1 O2 (16.1 kJ mol<sup>-1</sup>), and O4 (17.5 kJ mol<sup>-1</sup>), in quantitative agreement with previous calculations and in qualitative agreement with neutron diffraction occupancies. A new local minimum denoted O2\* (31.4 kJ mol<sup>-1</sup> relative to O3) was located, with a proton bound to O2 but pointing into the sodalite cage. Transition states between each pair of minima were fully characterized, yielding ZPE corrected activation energies ranging from 35.5 to 123.4 kJ mol<sup>-1</sup>. No correlation was found between barrier height and local structure; we considered 10 structural parameters including ring size, T–O–T angle, and nonbonded oxygen distance. Total mean rate coefficients were found to exhibit a strong non-Arrhenius temperature dependence, with apparent activation energies in the range of ca. 60–100 kJ mol<sup>-1</sup> at high temperature, and ca. 3 kJ mol<sup>-1</sup> at low temperature. This low-temperature value reflects thermally assisted tunneling to a site with a slightly higher energy. NMR experiments by Sarv et al. and Ernst et al. report apparent activation energies of 61 and 78 kJ mol<sup>-1</sup>, respectively, extracted from temperature ranges 298–658 and 610–640 K. Our theoretically computed apparent activation energies for these temperature ranges are 72 and 79 kJ mol<sup>-1</sup>, respectively, in quite good agreement with experiment.

## I. Introduction

Zeolites are used as shape-selective catalysts in a variety of important petrochemical processes such as cracking and reforming,<sup>1</sup> and also find use in the production of biofuels and bioproducts.<sup>2,3</sup> The activity of zeolite catalysts is often associated with Brønsted acid sites, which have the form ≡Si–OH–Al≡.<sup>4,5</sup> Studying internal proton transfer in bare zeolites is important for understanding the dynamical onset of catalytic activity through the redistribution of protons from small to large cages. Despite the many outstanding computational and experimental studies of proton siting and motion, we still lack the kind of quantitative agreement between experiment and theory that comes with complete understanding of the problem. This lack of agreement is remarkable given the relatively well-defined structures offered by zeolites. For example, NMR measurements of proton motion in bare H–Y by Sarv et al.<sup>6</sup> and by Ernst et al.<sup>7</sup> yield apparent activation energies of 61 and 78 kJ mol<sup>-1</sup>, respectively, extracted from temperature ranges 298–658 and 610–640 K. The physical origin of this discrepancy remains unclear. Ryder et al. suggest that residual water can influence proton-transfer barriers.<sup>8</sup> In this article, we report proton-transfer rate calculations indicating that acid site heterogeneity and quantum tunneling provide an alternative explanation for the difference.

NMR measurements of proton motion in solids typically extract correlation times,  $\tau_c$ , from relaxation<sup>7</sup> or other variable-temperature observations.<sup>6</sup> These correlation times control the decay rates of orientational correlation functions of the proton's magnetic moment.<sup>9</sup> This decay is generally influenced by all possible site-to-site proton jumps, such as those around the oxygens of an AlO<sub>4</sub> tetrahedron in zeolite H–Y, as shown in Figure 1. For structures exhibiting sufficiently high symmetry such as tetrahedral symmetry, the orientational correlation time is given by the inverse of the unique proton jump rate constant.<sup>10</sup> Because the four oxygens in H–Y are not crystallographically identical,<sup>11</sup> proton hopping in H–Y is close to but not exactly tetrahedral. When symmetry is broken by such structural heterogeneity, the total mean rate constant  $\langle k \rangle$  becomes a useful approximation for the inverse correlation time.<sup>12</sup> The total mean rate is given by  $\sum_{i \neq f} P_i k_{i \rightarrow f}$ , where  $P_i$  is the probability of protonating site  $i$  and  $\{k_{i \rightarrow f}\}$  are the site-to-site rate coefficients. Assuming that  $\tau_c \propto 1/\langle k \rangle$  is the *ansatz* of the present article. In a forthcoming article, we will rigorously consider the effects of structural heterogeneity through kinetic Monte Carlo simulations of orientational correlation functions,<sup>10,12</sup> parametrized by the rate coefficients presented below.

We compute proton-transfer energies by embedding small quantum clusters in larger classical clusters using ONIOM as implemented in Gaussian03.<sup>13</sup> A very similar approach was reported by Sierka and Sauer in 2001 for proton transfer in H–Y, H–ZSM-5, and H–chabazite.<sup>14</sup> Sierka and Sauer reported rate coefficients obtained with classical transition state theory; below we include quantum tunneling into our rate

\* Corresponding author. E-mail: auerbach@chem.umass.edu.

<sup>†</sup> Department of Chemistry, University of Massachusetts Amherst.

<sup>‡</sup> Department of Chemical Engineering, University of Massachusetts Amherst.

<sup>§</sup> Gaussian, Inc.

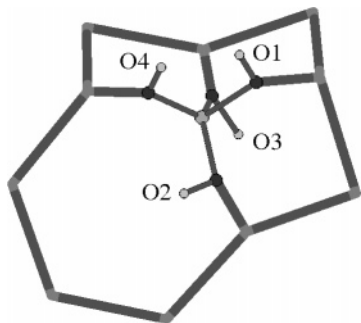


**Figure 1.** Schematic of four distinct proton sites in H–Y zeolite. Faster proton transfer among these sites leads to orientational randomization probed by NMR.

calculations by using truncated harmonic semiclassical rate theory.<sup>15</sup> We show below that tunneling manifests itself through strongly non-Arrhenius character of the total mean rate. With respect to the potential energy landscape, our results mirror those of Sierka and Sauer except for one interesting detail. Although they report a direct jump between sites at O3 (inside double 6-ring) and O2 (supercage 6-ring), our analysis finds no such direct process because of the intervening aluminum atom. Instead, we find a direct process from O3 to a modified O2 site, denoted O2\*, which points into the sodalite cage. Such a site has not been reported by neutron diffraction,<sup>11</sup> perhaps because of its low symmetry, relatively high energy, and low barrier to reaching the O2 site. The properties of the O3 ↔ O2\* jump detailed below resemble closely those of the O3 ↔ O2 process reported by Sierka and Sauer.<sup>14</sup> The Al–H angle subtended during the O3 ↔ O2\* process turns out to be quite a bit smaller than the tetrahedral angle, making this jump less important than the others for orientational randomization. This is nonetheless an intriguing jump process. Below, we consider the total mean rate in the presence and absence of this new jump, to explore its effect on the overall proton-transfer dynamics.

Thermally assisted tunneling blends classical activation with quantum tunneling. We find below that thermally assisted tunneling controls proton motion in H–Y at low temperatures, producing a small residual apparent activation energy associated with endothermic jumps. At high temperatures, we find apparent activation energies in the 60–100 kJ mol<sup>-1</sup> range, depending on the temperature window. These apparent activation energies reflect complicated averages of fundamental barriers in the approximate range 40–120 kJ mol<sup>-1</sup>. With such a range of barriers, one might expect a clear correlation between barrier height and a local structural parameter. Such a correlation would provide a convenient yardstick for estimating time scales of proton motion in other zeolites. Below we report that no correlation was found between barrier height and local structure. We considered 10 structural parameters including ring size, T–O–T angle, and nonbonded oxygen distance at the transition state. We do find, however, nearly quantitative agreement with the NMR experiments of Sarv et al.<sup>6</sup> and Ernst et al.,<sup>7</sup> finding that the difference in their activation energies comes from the strongly non-Arrhenius temperature dependence of the total mean proton-transfer rate.

The remainder of this article is organized as follows: Section II.A outlines the semiclassical rate theory used to evaluate elementary rates; Section II.B describes the electronic structure methods used to parametrize the semiclassical rate theory. The results of the electronic structure calculations are summarized in Section III.A; in Section III.B, we describe the dynamics of

proton motion with comparisons to experimental data; and in Section IV we offer concluding remarks.

## II. Methods

Here we describe the computational methods used to model the structure and dynamics of protons in H–Y zeolite. We apply direct dynamics calculations, where rate coefficients are obtained immediately from electronic structure data. First we outline the rate calculation, indicating the necessary input energies and frequencies; then we describe the electronic structure calculations of these input parameters.

**A. Kinetic Rate Calculations.** The total mean rate, which is the average over all proton-transfer processes, is obtained by combining the statistical probabilities for protonating each oxygen, with the rates for all possible transitions between sites. In H–Y zeolite, there are four crystallographically distinct oxygens,<sup>11</sup> and hence four different proton sites denoted O1, O2, O3, and O4 (below we consider a fifth site denoted O2\*). The expression for the total mean rate is thus given by

$$\langle k \rangle = \sum_i \sum_{f \neq i} P_i k_{i \rightarrow f} \quad \text{where} \quad P_i = \frac{Q_i}{\sum_j Q_j} \quad (1)$$

The double sum in eq 1 runs over all forward and reverse proton jumps, which by detailed balance contribute equally to the total mean rate.  $P_i$  is the statistical probability for the proton to occupy site  $i$ ; this equilibrium probability is proportional to  $Q_i$ , the partition function for site  $i$ .  $k_{i \rightarrow f}$  is the temperature-dependent elementary rate coefficient for transfer from site  $i$  to  $f$ .

We compute each  $k_{i \rightarrow f}(T)$  using truncated harmonic semiclassical transition state theory (SC-TST),<sup>15,16</sup> which gives the rate as a product of the harmonic TST rate coefficient (without tunneling),  $k_{i \rightarrow f}^{\text{TST}}$ , and a tunneling correction factor  $\Gamma_{i \rightarrow f}$ . More details regarding SC-TST can be found in refs 15 and 16. The SC-TST rate is thus given by

$$k_{i \rightarrow f}^{\text{SC-TST}}(T) = k_{i \rightarrow f}^{\text{TST}}(T) \cdot \Gamma_{i \rightarrow f}(T), \quad \text{where} \quad (2)$$

$$k_{i \rightarrow f}^{\text{TST}}(T) = \frac{k_B T}{h} \frac{Q_{i \rightarrow f}^\ddagger}{Q_i} = \frac{k_B T}{h Q_i} \sum_{n_i^\ddagger} \exp \left\{ -\beta \left[ V^\ddagger + \sum_{i=1}^{F-1} \hbar \omega_i^\ddagger \left( n_i^\ddagger + \frac{1}{2} \right) \right] \right\}, \quad \text{and} \quad (3)$$

$$\Gamma_{i \rightarrow f}(T) = \left[ \frac{e^{\beta \Delta E_0^\ddagger}}{1 + e^{2\pi \Delta E_0^\ddagger / \hbar |\omega_q^\ddagger|}} + \frac{1}{2} \int_{-\infty}^{\pi \Delta E_0^\ddagger / \hbar |\omega_q^\ddagger|} d\theta e^{\beta \hbar |\omega_q^\ddagger| \theta / \pi} \operatorname{sech}^2 \theta \right] \quad (4)$$

In eqs 1–4, each  $Q$  is a reactant or transition state partition function computed as a product of one-dimensional quantum-harmonic partition functions,  $\Delta E_0^\ddagger$  is the zero-point energy (ZPE) corrected barrier height for the  $i$  to  $f$  transition,  $\beta = (1/k_B T)$ , and  $\omega_q^\ddagger$  is the imaginary frequency of the reaction coordinate  $q$  at the  $i \leftrightarrow f$  transition state. Because  $\omega_q^\ddagger$  controls the curvature and hence the width of the barrier, it is the single parameter that most influences tunneling probabilities.

SC-TST provides a useful rate theory for studying tunneling in complex systems such as zeolites because it offers a balance between accuracy and ease of parametrization. Because this version of SC-TST relies on a separable harmonic approxima-

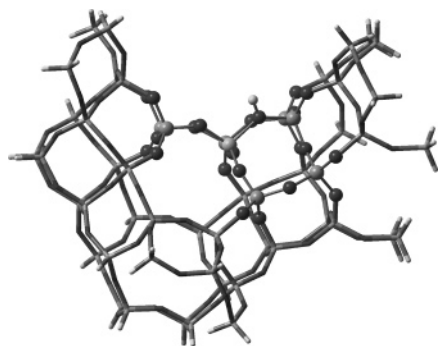


**Figure 2.** 8T–53T embedded cluster. Atoms represented as balls are included in the quantum cluster (C) treated by B3LYP/6-311G(d,p). Atoms represented as sticks are included in the outer layer and are treated with the universal force field.

tion,<sup>16</sup> the theory overestimates tunneling probabilities due to neglect of barrier anharmonicity. Alternatively, the theory also underestimates tunneling probabilities because it ignores corner-cutting paths that shorten tunneling paths. Although we cannot expect these two approximations to cancel exactly, their partial cancellation certainly reduces overall error. Considering that truncated harmonic SC-TST only requires electronic energies and frequencies at reactant and transition states, and that SC-TST smoothly connects the proper high- and low-temperature limits,<sup>15</sup> this rate theory is the most robust given the limited amount of electronic structure data required.

**B. Electronic Structure Calculations.** We compute proton-transfer energies by performing quantum chemistry calculations on large but finite clusters in the gas phase, without periodic boundary conditions. Although lattice summations such as the Ewald sum are crucial for computing deprotonation energies in zeolites, we have shown in ref 13 that finite clusters yield smooth convergence of proton-transfer energies. This is because slowly varying contributions to electrostatic energies essentially cancel when computing energy differences between nearby proton configurations.

The parameters needed for rate calculations were obtained using the Gaussian03 suite of quantum chemistry programs.<sup>17</sup> In previous work, we reported that an efficient and straightforward computational approach for obtaining converged energies and frequencies is a two-layer ONIOM<sup>18–21</sup> calculation with the total system (S) partitioned into an inner layer (I) containing 8 tetrahedrally coordinated atoms and an outer layer (O) containing an additional 45 tetrahedrally coordinated atoms, which we designate an 8T–53T system.<sup>13</sup> In these calculations, we did not include electrostatic interactions between the inner and outer layers; that is, we performed mechanical embedding but not electronic embedding. Dangling bonds at the interface of the inner layer (I) are saturated with hydrogen link atoms; the inner layer plus link atoms yields the cluster (C) on which electronic structure calculations are performed. The 8T–53T two-layer system is shown in Figure 2, where the proton is located at site O1.

The ONIOM energy of the total system is then approximated as

$$E_{\text{embed}} = E_{\text{lo}}(S) + [E_{\text{hi}}(C) - E_{\text{lo}}(C)] = E_{\text{hi}}(C) + [E_{\text{lo}}(S) - E_{\text{lo}}(C)] \quad (5)$$

where the subscripts indicate a lower (lo) or higher (hi) level of theory applied to the cluster (C) or total system (S).

In eq 5, the first form suggests a low-level treatment of the entire system corrected by a high-level treatment of the reacting

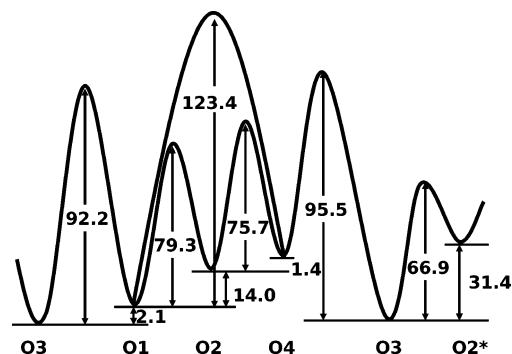


**Figure 3.** Schematic potential energy surface with all local minima and elementary jump processes. The site O3 is the ground state of the system. O2\* is the newly identified site with the highest energy of all sites.

center, while the second (mathematically identical) form suggests a quantum cluster calculation corrected with a low-level treatment of long-range effects. In our work, the inner layer ( $E_{\text{hi}}(C)$ ) is described with a full electronic structure calculation using the B3LYP functional and a 6-311G(d,p) split valence basis set.<sup>22–24</sup> Steric effects that enforce the overall shape while allowing realistic flexibility of the reacting cluster are provided by embedding the inner layer into an extended framework of atoms described by the universal force field (UFF) molecular mechanics potential function.<sup>25</sup> The terminal atoms of the outer layer are frozen at their crystallographically determined locations to constrain the system as if it were part of a macroscopic zeolite crystal.<sup>11</sup>

This layered combination of DFT and UFF has shown good convergence of reaction energies, barriers, and frequencies with respect to cluster and system size.<sup>13</sup> We expect this model chemistry to predict structural parameters and reaction energies to chemical accuracy, vibrational frequencies to within 200  $\text{cm}^{-1}$ , and to underestimate activation energies by about 10%.<sup>26</sup>

### III. Results and Discussion

**A. Potential Energy Landscape.** Figure 3 illustrates the reaction and activation energies of all proton jumps around an  $\text{AlO}_4$  tetrahedron in H–Y zeolite. In our model chemistry, a proton at site O3 is the most thermodynamically stable (least acidic) and a proton at O4 is the least stable (most acidic). The general ordering of stability,  $\text{O3} > \text{O1} \gg \text{O2} > \text{O4}$ , agrees qualitatively with all other published studies, both experimental and theoretical,<sup>27–30</sup> although the ordering of the two lowest energy sites, which differ by about 2  $\text{kJ mol}^{-1}$ , varies from one study to the next. Our results also reveal a larger range in ZPE-corrected barrier heights than that reported previously by Sierka and Sauer for H–Y.<sup>14</sup> In particular, our  $\text{O1} \rightarrow \text{O4}$  barrier is about 25  $\text{kJ mol}^{-1}$  higher than that of Sierka and Sauer. In previous work, we attributed this difference to a combination of basis set effects and termination/volume constraints.<sup>13</sup> The other barriers in Figure 3 are in excellent agreement with the calculations of Sierka and Sauer. Because the  $\text{O1} \rightarrow \text{O4}$  barrier is the largest in this system, its influence on the total mean rate is relatively small except at the highest temperatures considered.

Another difference between our results and those of Sierka and Sauer concerns the  $\text{O2} \leftrightarrow \text{O3}$  process. Although they report a direct jump between sites at O3 (inside double 6-ring) and O2 (supercage 6-ring), our analysis finds no such direct process because of the intervening aluminum atom. Nonetheless, Sierka and Sauer report an  $\text{O3} \rightarrow \text{O2}$  barrier of 68.3  $\text{kJ mol}^{-1}$ , making it their lowest barrier for proton motion in H–Y. To explore this discrepancy, we traced the minimum energy pathway (MEP)

**TABLE 1: Key Dynamical Parameters for Semiclassical Rate Theory**

	$\Delta E_0$ (kJ mol <sup>-1</sup> )	$\Delta E_0^\ddagger$ (kJ mol <sup>-1</sup> )	$ \bar{\nu}_q^\ddagger $ (cm <sup>-1</sup> )	$\mu_q^\ddagger$ (amu)
O3 $\rightarrow$ O2*	31.4	66.9	1347.0	1.11
O2 $\rightarrow$ O4	1.4	75.7	1455.5	1.08
O1 $\rightarrow$ O2	14.0	79.3	1185.0	1.16
O3 $\rightarrow$ O1	2.1	90.1	1072.4	1.21
O3 $\rightarrow$ O4	17.5	95.5	991.3	1.27
O1 $\rightarrow$ O4	15.4	123.4	1621.2	1.06

descending from the reported transition state of Sierka and Sauer to its eventual reactant and product sites. These sites turn out to be O3 and a modified O2 site, denoted O2\*, which points into the sodalite cage because the O3–Al–O2–H torsional angle is rotated by ca. 15°. We find the O2\* local minimum to be 15.3 kJ mol<sup>-1</sup> higher in energy than the traditional O2 site because the AlO<sub>4</sub> tetrahedron is significantly distorted (angles ranging from 87 to 120°). Such a site has not been reported by neutron diffraction,<sup>11</sup> perhaps because of its low symmetry and high energy. The properties of the O3  $\leftrightarrow$  O2\* jump shown in Figure 3 resemble closely those of the O3  $\leftrightarrow$  O2 process reported by Sierka and Sauer. Indeed, our O3  $\rightarrow$  O2\* barrier is 66.9 kJ mol<sup>-1</sup>, very close to 68.3 kJ mol<sup>-1</sup> reported previously.<sup>14</sup> Thus, the motion of a proton between sites O2 and O3 is actually a two-step process mediated by O2\*, an intermediate site 31.4 kJ mol<sup>-1</sup> above the global minimum at O3.

Table 1 lists the key dynamical parameters used to compute SC-TST rate coefficients. For sufficiently simple systems, for example, quartic double wells, one would expect a correlation between barrier height and barrier curvature; pathways that reach higher-energy transition states would be correspondingly steeper near the saddle point. The data in Table 1 are ordered by increasing barrier, making it clear that there is no such correlation between barrier height and curvature, in this case expressed as the imaginary frequency of the reaction coordinate at the transition state,  $|\bar{\nu}_q^\ddagger|$ . This is because framework distortions influence the various proton jump pathways to different extents, as illustrated by the variation in reaction-coordinate reduced masses shown in Table 1.

The data in Table 1 allow us to intuitively anticipate some of the dynamics results below. From classically activated proton motion, we expect an apparent activation energy at high temperatures between 67 and 80 kJ mol<sup>-1</sup> because all sites may be sampled via pathways that have activation energies in that range relative to the global minimum. To assess the importance of quantum tunneling, the approximation

$$T_x \simeq \frac{\hbar|\omega_F^\ddagger|}{2\pi k_B} \quad (6)$$

allows a base-case estimate of the tunneling crossover temperature ( $T_x$ ), the temperature below which tunneling is very important and a quantum rate theory is required.<sup>15</sup> These crossover temperatures fall between 228 K for the O3  $\leftrightarrow$  O4 process and 373 K for the O1  $\leftrightarrow$  O4 process, suggesting that tunneling influences proton-transfer dynamics at temperatures probed by many experiments.

**B. Proton-Transfer Dynamics.** The temperature dependence of the total mean rate is shown in Figures 4 and 5. These figures contain results that differ in their treatment of the O2\* site. On the one hand, our discovery of the O3  $\leftrightarrow$  O2\* process warrants its inclusion in the total mean rate. On the other hand, the angle subtended by the Al–H vector during this process is relatively small ( $\sim 44^\circ$ ), making this jump less important than the others for orientational randomization, and hence for modeling NMR

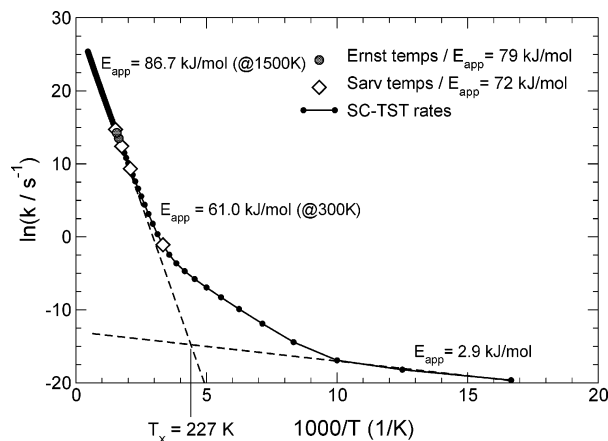


**Figure 4.** Temperature dependence of the total mean rate when neglecting O3  $\leftrightarrow$  O2\* processes. Ten elementary steps combine to give the total mean rate, from which we extract apparent activation energies from various temperature ranges. Excellent agreement is obtained comparing our apparent activation energies to those of Sarv et al. and Ernst et al.

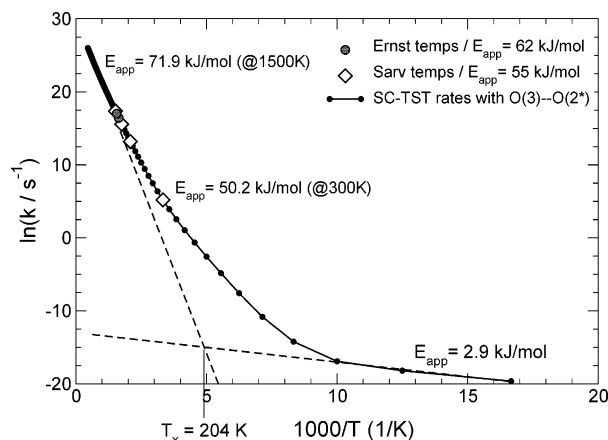


**Figure 5.** Temperature dependence of the total mean rate when including O3  $\leftrightarrow$  O2\* processes. Twelve elementary steps combine to give the total mean rate, from which we extract apparent activation energies from various temperature ranges. More pronounced non-Arrhenius temperature dependence is seen at higher temperatures from including O3  $\leftrightarrow$  O2\* processes.

dynamics. We expect that by ignoring this process (Figure 4) and including the process (Figure 5) we will bracket the correct answer, which lies somewhere in between. In a forthcoming article, we will rigorously consider the importance of the O3  $\leftrightarrow$  O2\* process by performing kinetic Monte Carlo simulations of orientational correlation functions,<sup>10,12</sup> parametrized by the rate data reported herein.

We begin by examining Figure 4, which neglects the O3  $\leftrightarrow$  O2\* pathway. We see in Figure 4 a strongly non-Arrhenius temperature dependence, with distinct behaviors in the low- and high-temperature regimes. This is to be expected for a system that exhibits both quantum tunneling at low temperatures and activated barrier crossing at high temperatures. Quantum tunneling manifests itself at low temperatures through rate constants that are nearly independent of temperature. In Figure 4 we see a small, residual apparent activation energy in the low-temperature regime, signaling thermally assisted tunneling. This mechanism appears for endothermic tunneling processes: the reactant must be activated by the ZPE-corrected reaction energy before tunneling to product may proceed. The apparent activation energy in Figure 4, 2.9 kJ mol<sup>-1</sup>, is quite close to 2.1 kJ mol<sup>-1</sup>, the ZPE-corrected reaction energy for O3  $\rightarrow$  O1.

Thermally assisted tunneling from O3 to O1 thus dominates the total mean rate at low temperatures.

As we move to the high-temperature regime in Figure 4, in which classically activated proton transfer dominates, we see the progressive increase of the apparent activation energy with increasing temperature. This regime also exhibits a non-Arrhenius temperature dependence because of acid site heterogeneity contributing many distinct classical rate processes (see below for a discussion of the dominating processes). To illustrate this, we computed local apparent activation energies at 300 and 1500 K, finding 61.0 to 86.7 kJ mol<sup>-1</sup>, respectively. In general, we find that the non-Arrhenius temperature dependence from tunneling is much stronger than that from classical acid site heterogeneity.

To make direct contact with the NMR dynamics experiments of Sarv et al.<sup>6</sup> and Ernst et al.,<sup>7</sup> we evaluated total mean rates at the temperatures used in these studies for the calculation of experimental apparent activation energies. These temperatures are 298, 478, 568, and 658 K for Sarv et al., and 610, and 640 K for Ernst et al. As shown in Figure 4, the apparent activation energies extracted from these theoretical total mean rates are  $E_{\text{app}} = 72$  kJ mol<sup>-1</sup> for the Sarv temperatures and  $E_{\text{app}} = 79$  kJ mol<sup>-1</sup> for the Ernst temperatures. The latter result is in quantitative agreement with the 78 kJ mol<sup>-1</sup> reported by Ernst et al. Such quantitative agreement between theory and experiment may be unprecedented for proton dynamics in zeolites.

Sarv et al. report an apparent activation energy of  $61 \pm 1$  kJ mol<sup>-1</sup> from their variable-temperature MAS NMR experiment.<sup>6</sup> The tight error bars reported with this number prompted us to revisit the analysis of their raw data. Beginning with their raw values of the second moment of the MAS NMR line width (so-called “M2” in their paper) and the graphically reported error bars, we computed NMR correlation times using eqs 2–4 in their paper,<sup>6</sup> from which we extracted an apparent activation energy using statistical analysis software.<sup>31</sup> If we do *not* use their published error bars in propagating error through to the apparent activation energy, then we obtain  $61.5 \pm 5.8$  kJ mol<sup>-1</sup>, in very good agreement with their reported value, but with larger error bars. In contrast, if we *do* incorporate their M2 error bars in the regression analysis, then we obtain  $68.0 \pm 12$  kJ mol<sup>-1</sup>. We believe this latter result more correctly reflects their experimental results. This value agrees quite well with our theoretical result of 72 kJ mol<sup>-1</sup>, once again showing nearly quantitative agreement between theory and experiment for proton motion in this system. (We cannot re-evaluate the regression analysis of Ernst et al. because they fit a line to two points.)

Our results suggest that the difference between the apparent activation energies of Sarv et al. and Ernst et al. is caused by quantum tunneling. Indeed, if we repeat all of the above total mean rate calculations *without* including tunneling (i.e., set  $\Gamma = 1$  in all rates), we find theoretical apparent activation energies corresponding to the Sarv and Ernst temperature ranges of 82.1 and 84.0 kJ mol<sup>-1</sup>, respectively. Given the magnitude of the experimental error bars, these would be regarded as the same number. In general, when tunneling is important, we expect apparent activation energies to decrease as the probed temperatures decrease.

The intersection between tangent lines in Figure 4 extracted at high and low temperatures gives a tunneling crossover temperature,  $T_x$ , broadly interpreted as the temperature below which tunneling becomes important. This crossover arising from the total mean rate is much less sharply defined than that for an elementary process. At the crossover temperature 227 K in

**TABLE 2: Contributions ( $P_i k_{i \rightarrow j}$ ) to the Total Mean Rate from Each Elementary Process When Neglecting  $\text{O3} \leftrightarrow \text{O2}^*$  <sup>a</sup>**

$T$ (K)	$\text{O2} \rightarrow \text{O4}$	$\text{O1} \rightarrow \text{O2}$	$\text{O3} \rightarrow \text{O1}$	$\text{O3} \rightarrow \text{O4}$	$\text{O1} \rightarrow \text{O4}$
200	$3.66 \times 10^{-4}$	$1.25 \times 10^{-4}$	$2.77 \times 10^{-7}$	$6.25 \times 10^{-10}$	$6.38 \times 10^{-8}$
500	$1.56 \times 10^3$	$9.34 \times 10^3$	$9.94 \times 10^2$	$3.49 \times 10^2$	$4.64 \times 10^{-1}$
800	$3.21 \times 10^6$	$8.78 \times 10^6$	$2.76 \times 10^6$	$1.32 \times 10^6$	$1.75 \times 10^4$

<sup>a</sup> By detailed balance, each reverse process contributes a term exactly equal to the forward process. Note that the  $\text{O2} \rightarrow \text{O4}$  and  $\text{O1} \rightarrow \text{O2}$  processes dominate at low to medium temperatures.

Figure 4, the total mean rate is  $10^4$  times larger than the corresponding classical rate. This crossover temperature of the total mean rate lies at the bottom end of the range for the 10 elementary processes considered, showing that the effective averaging of elementary crossover temperatures is highly nonlinear.

The temperature dependence of the total mean rate including  $\text{O3} \leftrightarrow \text{O2}^*$  processes is shown in Figure 5. In general, all of the above conclusions remain qualitatively valid; the numerical values of apparent activation energies do, however, shift. Figure 5 shows an even more pronounced non-Arrhenius temperature dependence in the mid- to high-temperature regimes. Including  $\text{O3} \leftrightarrow \text{O2}^*$  processes gives apparent activation energies at 300 and 1500 K of 50 and 62 kJ mol<sup>-1</sup>, respectively. These values are significantly lower than those observed before because the  $\text{O3} \rightarrow \text{O2}^*$  barrier, 66.9 kJ mol<sup>-1</sup>, is the lowest in the system. Comparing again with the NMR data of Sarv and Ernst, we get apparent activation energies of 55 and 62 kJ mol<sup>-1</sup>, respectively, when including  $\text{O3} \leftrightarrow \text{O2}^*$ . As stated above, this jump is less important than the others because the angle subtended by the Al–H vector during this process is relatively small. In a forthcoming article, we will rigorously consider the importance of the  $\text{O3} \leftrightarrow \text{O2}^*$  process by performing kinetic Monte Carlo simulations of orientational correlation functions,<sup>10,12</sup> parametrized by these rate data.

Although we stress the importance of including all possible proton jumps, it is interesting to ask whether a small subset of jumps dominates proton motion in H–Y zeolite. Tables 1 and 2 show these individual contributions ( $P_i k_{i \rightarrow j}$ ) when neglecting and including  $\text{O3} \leftrightarrow \text{O2}^*$ , respectively. When neglecting  $\text{O3} \leftrightarrow \text{O2}^*$ , we find that up to 500 K the  $\text{O2} \leftrightarrow \text{O1}$  and  $\text{O2} \leftrightarrow \text{O4}$  processes dominate all others by several orders of magnitude. Although the fractional occupancy of site O3 is still relatively large at intermediate temperatures, the high and wide barriers connecting  $\text{O3} \leftrightarrow \text{O1}$  and  $\text{O3} \leftrightarrow \text{O4}$  strongly inhibit proton motion from the double 6-ring (O3) to the supercage (O1, O4). The NMR dynamics can thus be attributed to proton jumps between sites O1 and O4 via O2. When including  $\text{O3} \leftrightarrow \text{O2}^*$  (Table 2), this process becomes the lowest energy pathway of all and dominates up to elevated temperatures. This provides a qualitatively different interpretation of the NMR dynamics. Orientational correlation function calculations will help shed light on which interpretation is correct.

We report herein site-to-site proton-transfer barriers that cover a remarkably broad range: roughly 60–120 kJ mol<sup>-1</sup> when ignoring  $\text{O3} \leftrightarrow \text{O2}^*$ , and 40–120 kJ mol<sup>-1</sup> when including it. With such a range of barriers, one might expect a clear correlation between barrier height and a local structural parameter. Such a correlation would provide a convenient yardstick for estimating time scales of proton motion in other zeolites. We considered 10 structural parameters including (1) ring size, (2) T–O–T angle, (3) proton donor–acceptor distance at the transition state, and (4) closest nonbonded oxygen distance at

**TABLE 3: Contributions ( $P_i k_{i \rightarrow j}$ ) to the Total Mean Rate from Each Elementary Process When Including  $O3 \leftrightarrow O2^*$  <sup>a</sup>**

<i>T</i> (K)	$O3 \rightarrow O2^*$	$O2 \rightarrow O4$	$O1 \rightarrow O2$	$O3 \rightarrow O1$	$O3 \rightarrow O4$	$O1 \rightarrow O4$
200	$3.80 \times 10^{-2}$	$3.66 \times 10^{-4}$	$1.2 \times 510^{-4}$	$2.77 \times 10^{-7}$	$6.25 \times 10^{-10}$	$6.38 \times 10^{-8}$
500	$4.73 \times 10^5$	$1.56 \times 10^3$	$9.34 \times 10^3$	$9.94 \times 10^2$	$9.94 \times 10^2$	$4.64 \times 10^{-1}$
800	$1.14 \times 10^8$	$3.20 \times 10^6$	$8.75 \times 10^6$	$2.75 \times 10^6$	$2.75 \times 10^6$	$1.74 \times 10^4$

<sup>a</sup> By detailed balance, each reverse process contributes a term exactly equal to the forward process. Note that the  $O3 \leftrightarrow O2^*$  process dominates for all temperatures shown.

the transition state. In all, we considered structural parameters involving two-body to five-body motions. Remarkably, none of these structural parameters were found to correlate with our computed barrier heights. We did find, in agreement with Sierka and Sauer,<sup>14</sup> that the lowest barriers arise for proton motion in 6-membered rings; however, the cause remains unclear. We do suggest a possible reason why the  $O1 \rightarrow O4$  barrier (123.4 kJ mol<sup>-1</sup>) is so high. This process occurs roughly in the plane of the 12-ring window. As such, the transition state involves a proton in “free space,” that is, relatively far from potentially stabilizing framework atoms. Unfortunately, extending these ideas to correlating the other jumps was unsuccessful. This suggests that the energetics of proton transfer in zeolites is inherently complicated by cooperative motions involving more than just a handful of atoms.

#### IV. Summary and Concluding Remarks

We have computed the total mean rate coefficient for proton transfer in bare H–Y zeolite, for comparison with NMR experiments and previous calculations. Studying internal proton transfer in bare zeolites is important for understanding the dynamical onset of catalytic activity through the redistribution of protons from small to large cages. We computed proton-transfer energies using two-layer ONIOM calculations on an 8T–53T cluster, where *x*T indicates *x* tetrahedral atoms. Rate coefficients were computed using truncated harmonic semiclassical transition state theory. The zero-point energy (ZPE) corrected proton site energies in H–Y (FAU structure) were found to be O3 (0 kJ mol<sup>-1</sup>), O1 (2.1 kJ mol<sup>-1</sup>), O2 (16.1 kJ mol<sup>-1</sup>), and O4 (17.5 kJ mol<sup>-1</sup>), in quantitative agreement with previous calculations and in qualitative agreement with neutron diffraction occupancies. A new local minimum denoted O2\* (31.4 kJ mol<sup>-1</sup> relative to O3) was located, with a proton bound to O2 but pointing into the sodalite cage. Such a site has not been reported by neutron diffraction, perhaps because of its low symmetry and high energy. Transition states between each pair of minima were fully characterized, yielding ZPE-corrected activation energies ranging from 35.5 to 123.4 kJ mol<sup>-1</sup>. No correlation was found between barrier height and local structure; we considered 10 structural parameters including ring size, T–O–T angle, and nonbonded oxygen distance.

Total mean rate coefficients were found to exhibit a strong non-Arrhenius temperature dependence, with apparent activation energies in the range of ca. 60–100 kJ mol<sup>-1</sup> at high temperature, and ca. 3 kJ mol<sup>-1</sup> at low temperature. This low-temperature value reflects thermally assisted tunneling to a site with slightly higher energy. NMR experiments by Sarv et al. and Ernst et al. report apparent activation energies of 61 and 78 kJ mol<sup>-1</sup>, respectively, extracted from temperature ranges 298–658 and 610–640 K. We reanalyzed the raw NMR data of Sarv et al., yielding a revised apparent activation energy of 68 kJ mol<sup>-1</sup>. Our theoretically computed apparent activation energies for these temperature ranges are 72 and 79 kJ mol<sup>-1</sup>, respectively, in quite good agreement with experiment. Our results suggest that the difference between the apparent activation energies of Sarv et al. and Ernst et al. is caused by the

different temperature ranges they study, which changes the relative importance of proton tunneling. This interpretation differs from that reported by Ryder et al., who suggest that residual water can influence proton-transfer barriers.<sup>8</sup> More research may be necessary to determine which interpretation is closer to the truth. In any event, the treatment of all possible proton jumps, the inclusion of quantum tunneling, and the calculation of the total mean rate, provide the most accurate simulation to date of proton dynamics in zeolites.

**Acknowledgment.** We acknowledge generous funding from the National Science Foundation: CTS-0553577 (John Regalbuto) and Chemical Bonding Center CHE-0739227 (Raima Larter). We also thank Rush for inspiration.

#### References and Notes

- (1) *Handbook of Zeolite Science and Technology*; Auerbach, S. M., Carrado, K. A., Dutta, P. K., Eds.; Marcel Dekker, Inc.: New York, 2003.
- (2) Huber, G. W.; Iborra, S.; Corma, A. *Chem. Rev.* **2006**, *106*, 4044.
- (3) Corma, A.; Huber, G. W.; Sauvanaud, L.; O'Connor, P. *J. Catal.* **2007**, *247*, 307.
- (4) Rozanska, X.; van Santen, R. A. Reaction Mechanisms in Zeolite Catalysis. In *Handbook of Zeolite Science and Technology*; Auerbach, S. M., Carrado, K. A., Dutta, P. K., Eds.; Marcel Dekker, Inc.: New York, 2003.
- (5) Haw, J. F.; Marcus, D. M. Examples of Organic Reactions on Zeolites: Methanol to Hydrocarbon Catalysis. In *Handbook of Zeolite Science and Technology*; Auerbach, S. M., Carrado, K. A., Dutta, P. K., Eds.; Marcel Dekker, Inc.: New York, 2003.
- (6) Sarv, P.; Tuherm, T.; Lippmaa, E.; Keskinen, K.; Root, A. *J. Phys. Chem.* **1995**, *99*, 13763–13768.
- (7) Ernst, H.; Freude, D.; Mildner, T.; Pfeifer, H. High Temperature 1H MAS NMR Studies of Proton Mobility in Zeolites. In *Proceedings of the 12th International Zeolite Conference*; Treacy, M. M. J., Marcus, B. K., Bisher, M. E., Higgins, J. B., Eds.; MRS: Warrendale, PA, 1999; Vol. IV.
- (8) Ryder, J. A.; Chakraborty, A. K.; Bell, A. T. *J. Phys. Chem. B* **2000**, *104*, 6998–7011.
- (9) Schmidt-Rohr, K.; Spiess, H. W. *Multidimensional Solid-State NMR and Polymers*; Academic Press: London, 1994.
- (10) Auerbach, S. M.; Metiu, H. I. *J. Chem. Phys.* **1997**, *106*, 2893–2905.
- (11) Czjzek, M.; Jovic, H.; Fitch, A. N.; Vogt, T. *J. Phys. Chem.* **1992**, *96*, 1535–1540.
- (12) Blanco, C.; Saravanan, C.; Allen, M.; Auerbach, S. M. *J. Chem. Phys.* **2000**, *113*, 9778–9787.
- (13) Fermann, J. T.; Moniz, T.; Kiowski, O.; McIntire, T. J.; Auerbach, S. M.; Vreven, T.; Frisch, M. J. *J. Chem. Theory Comput.* **2005**, *1*, 1232–1239.
- (14) Sierka, M.; Sauer, J. *J. Phys. Chem. B* **2001**, *105*, 1603–1613.
- (15) Fermann, J. T.; Auerbach, S. *J. Chem. Phys.* **2000**, *112*, 6787–6794.
- (16) Hernandez, R.; Miller, W. H. *Chem. Phys. Lett.* **1993**, *214*, 129.
- (17) Frisch, M. J.; Trucks, G. W.; Schlegel, H. B.; Scuseria, G. E.; Robb, M. A.; Cheeseman, J. R.; Montgomery, J. A., Jr.; Vreven, T.; Kudin, K. N.; Burant, J. C.; Millam, J. M.; Iyengar, S. S.; Tomasi, J.; Barone, V.; Mennucci, B.; Cossi, M.; Scalmani, G.; Rega, N.; Petersson, G. A.; Nakatsuji, H.; Hada, M.; Ehara, M.; Toyota, K.; Fukuda, R.; Hasegawa, J.; Ishida, M.; Nakajima, T.; Honda, Y.; Kitao, O.; Nakai, H.; Klene, M.; Li, X.; Knox, J. E.; Hratchian, H. P.; Cross, J. B.; Bakken, V.; Adamo, C.; Jaramillo, J.; Gomperts, R.; Stratmann, R. E.; Yazyev, O.; Austin, A. J.; Cammi, R.; Pomelli, C.; Ochterski, J. W.; Ayala, P. Y.; Morokuma, K.; Voth, G. A.; Salvador, P.; Dannenberg, J. J.; Zakrzewski, V. G.; Dapprich, S.; Daniels, A. D.; Strain, M. C.; Farkas, O.; Malick, D. K.; Rabuck, A. D.; Raghavachari, K.; Foresman, J. B.; Ortiz, J. V.; Cui, Q.; Baboul, A. G.; Clifford, S.; Cioslowski, J.; Stefanov, B. B.; Liu, G.; Liashenko, A.; Piskorz, P.; Komaromi, I.; Martin, R. L.; Fox, D. J.; Keith, T.; Al-Laham,

M. A.; Peng, C. Y.; Nanayakkara, A.; Challacombe, M.; Gill, P. M. W.; Johnson, B.; Chen, W.; Wong, M. W.; Gonzalez, C.; Pople, J. A. *Gaussian 03*, revision C.02; Gaussian, Inc.: Wallingford, CT, 2004.

(18) Vreven, T.; Morokuma, K. *J. Comput. Chem.* **2000**, *21*, 1419–1432.

(19) Vreven, T.; Morokuma, K.; Farkas, O.; Schlegel, H. B.; Frisch, M. J. *J. Comput. Chem.* **2003**, *24*, 760–769.

(20) Vreven, T.; Byun, K. S.; Komaromi, I.; Dapprich, S.; Montgomery, J. A.; Morokuma, K.; Frisch, M. J. *J. Chem. Theory Comput.* **2006**, *2*, 815–826.

(21) Vreven, T.; Frisch, M. J.; Kudin, K. N.; Schlegel, H. B.; Morokuma, K. *Mol. Phys.* **2006**, *104*, 701–714.

(22) Becke, A. D. *J. Chem. Phys.* **1993**, *98*, 5648.

(23) Lee, C.; Yang, W.; Parr, R. G. *Phys. Rev. B* **1988**, *37*, 785.

(24) Krishnan, R.; Binkley, J. S.; Seeger, R.; Pople, J. A. *J. Chem. Phys.* **1980**, *72*, 650.

(25) Rappe, A. K.; Casewit, C. J.; Colwell, K. S.; Goddard, W. A.; Skiff, W. M. *J. Am. Chem. Soc.* **1992**, *114*, 10024–10035.

(26) Fermann, J. T.; Blanco, C.; Auerbach, S. *J. Chem. Phys.* **2000**, *112*, 6779–6786.

(27) Hill, J.; Freeman, C. M.; Delley, B. *J. Phys. Chem. A* **1999**, *103*, 3772–3777.

(28) Schroder, K. P.; Sauer, J.; Leslie, M.; Catlow, C. R. A.; Thomas, J. M. *Chem. Phys. Lett.* **1992**, *188*, 320.

(29) Schroder, K. P.; Sauer, J. *J. Phys. Chem.* **1996**, *100*, 11043.

(30) Sierka, M.; Sauer, J. *J. Faraday Discuss* **1997**, *106*, 41.

(31) *Origin*, version 7.5; OriginLab Corporation: Northampton, MA, 2007.